

QUANTUM COMPUTING

Fault-tolerant detection of a quantum error

S. Rosenblum^{1,2,*†}, P. Reinhold^{1,2,*}, M. Mirrahimi^{2,3}, Liang Jiang^{1,2}, L. Frunzio^{1,2}, R. J. Schoelkopf^{1,2}

A critical component of any quantum error-correcting scheme is detection of errors by using an ancilla system. However, errors occurring in the ancilla can propagate onto the logical qubit, irreversibly corrupting the encoded information. We demonstrate a fault-tolerant error-detection scheme that suppresses spreading of ancilla errors by a factor of 5, while maintaining the assignment fidelity. The same method is used to prevent propagation of ancilla excitations, increasing the logical qubit dephasing time by an order of magnitude. Our approach is hardware-efficient, as it uses a single multilevel transmon ancilla and a cavity-encoded logical qubit, whose interaction is engineered in situ by using an off-resonant sideband drive. The results demonstrate that hardware-efficient approaches that exploit system-specific error models can yield advances toward fault-tolerant quantum computation.

In a fault-tolerant (FT) implementation of an error-corrected quantum circuit, the failure of a single component results in at most a correctable error in the output (I). Scalable quantum computation will require fault tolerance for every part of a logical circuit, including state preparation, gates, and measurements (2). The FT detection of quantum errors is a particularly crucial component, because this operation must be performed frequently in any encoded circuit. Errors are typically detected by mapping properties of the system, known as error syndromes, onto an ancillary system, which is subsequently measured.

Typically, non-fault-tolerance in a syndrome measurement arises from errors in the ancilla that propagate to the logical qubit, where they can cause uncorrectable errors. A common proposed strategy is to introduce multiple ancillae, each interacting with a restricted number of physical qubits that make up a single logical qubit ($3-6$). Although this may prevent ancilla errors from spreading in the system, it comes at the cost of an increased hardware overhead. Alternatively, in the Bacon-Shor subsystem approach (7), ancilla errors are allowed to accumulate in degrees of freedom that need not be monitored or corrected. Recently, this type of syndrome measurement was demonstrated in both trapped ions and superconducting qubits by using a four-qubit code that allows error detection but not error correction ($8, 9$).

We implement a FT error syndrome measurement by engineering symmetries in the system-ancilla interaction that make it invariant under the action of dominant ancilla errors, preventing

their propagation to the system in any form. The system-ancilla interaction is designed to commute with the dominant error operators, and thus errors occurring during the interaction are equivalent to errors occurring afterward. This form of protection, called error transparency (10), extends concepts related to decoherence-free subspaces (11) in order to realize FT operations.

We implement our FT syndrome measurement on a logical qubit encoded in a single three-dimensional superconducting cavity ($\omega_c/2\pi = 4.5$ GHz, $T_1^c = 1.1$ ms). We encode quantum information using the Schrödinger cat code ($12-14$), whose computational basis is given by $|C_\alpha\rangle$ and $|C_{i\alpha}\rangle$, which are superpositions of coherent states $|C_\alpha\rangle \propto |\alpha\rangle + |-\alpha\rangle$. In our implementation, we set $\alpha = \sqrt{2}$, resulting in a mean photon number of 2. The dominant cavity error, single-photon loss, causes the photon number parity of both code words to change from even to odd, without destroying the encoded information. Parity is therefore the error syndrome, and the information can be recovered if the number of parity jumps is faithfully measured. This requires parity measurements to be performed frequently relative to the single-photon loss rate. To measure the parity of the cavity, we dispersively couple the cavity to an ancilla transmon ($\omega_q/2\pi = 6.5$ GHz, $T_1^{eg} = 26$ μ s, $T_2^{eg} = 12$ μ s), which is measured by using a standard readout chain (see supplementary text 1). When we consider the first three levels of the ancilla ($|g\rangle, |e\rangle$, and $|f\rangle$), this dispersive interaction can be represented as (setting $\hbar = 1$)

$$\hat{H}_{\text{int}} = \chi_e \hat{a}^\dagger \hat{a} |e\rangle\langle e| + \chi_f \hat{a}^\dagger \hat{a} |f\rangle\langle f| \quad (1)$$

where \hat{a} is the cavity photon annihilation operator and χ_e, χ_f are the cavity frequency shifts for the respective ancilla states ($\chi_g = 0$ in this frame of reference, and in the absence of driving $\chi_e/2\pi =$

-93 kHz, $\chi_f/2\pi = -236$ kHz). Evolution under this interaction for a time $\pi/\chi_e = 5.4$ μ s maps the parity of the cavity onto the phase of a superposition $|g\rangle + |e\rangle$ in the ancilla. Performing Ramsey interferometry on the ancilla to determine this phase yields an effective quantum non-demolition measurement of the parity ($15, 16$). This parity measurement protocol was previously used to demonstrate error correction at the break-even point (17), where the error-corrected lifetime equals that of the best element of the system.

The main limitation of error-correction based on the scheme described above is logical errors induced by spontaneous relaxation of the ancilla during the parity mapping (17). This can be seen by considering a jump from $|e\rangle$ to $|g\rangle$ during the π/χ_e interaction time (Fig. 1A). Although such a jump prevents one from correctly determining the photon number parity, it also has the more harmful effect of completely dephasing the cavity. Because the jump time is nearly uniformly distributed between 0 and π/χ_e , the cavity acquires a phase space rotation uniformly distributed between 0 and π . This imposes an uncorrectable error with a probability proportional to the number of parity measurements performed. This cost forces the designer of an error correction protocol to measure the error syndrome less frequently than would otherwise be desirable and consequently reduces the potential achievable lifetime gain. More generally, the non-fault-tolerance of the traditional protocol arises because ancilla relaxation errors do not commute with the interaction Hamiltonian. In particular, the commutator of the interaction Hamiltonian with the associated collapse operator is $[\hat{H}_{\text{int}}, |g\rangle\langle e|] = -\chi_{eg} \hat{a}^\dagger \hat{a} |g\rangle\langle e|$ (where $\chi_{ij} = \chi_i - \chi_j$, for $i, j \in \{g, e, f\}$), which generates a nontrivial operation on the logical subspace and is therefore an uncorrectable error. In contrast, pure dephasing of the ancilla, which occurs at a comparable rate, does not result in unwanted cavity decoherence because the collapse operator ($|e\rangle\langle e|$) commutes with the interaction. Therefore, the end result of an ancilla dephasing event during the interaction is equivalent to an ancilla dephasing event after the interaction, which clearly does not affect the logical qubit. The parity measurement is therefore “transparent” with respect to ancilla dephasing (10).

We extend this error transparency to include relaxation by introducing a third level to the ancilla Hilbert space (Fig. 1B). This provides us with an additional degree of freedom, allowing us to maintain the system-ancilla interaction rate, while zeroing the rate of first-order error propagation. If we change our initial ancilla encoding to a superposition of $|g\rangle$ and $|f\rangle$ (instead of $|g\rangle$ and $|e\rangle$), the dominant error becomes relaxation from $|f\rangle$ to $|e\rangle$ (selection rules forbid direct $|f\rangle$ to $|g\rangle$ transitions). The commutator of this error ($|e\rangle\langle f|$) with the interaction Hamiltonian is $\chi_{fe} |e\rangle\langle f| \hat{a}^\dagger \hat{a}$. Because the measurement rate (which scales with χ_{fg}) is independent of the dephasing rate (which scales with χ_{fe}), it becomes feasible to maintain the measurement

¹Departments of Applied Physics and Physics, Yale University, New Haven, CT 06511, USA. ²Yale Quantum Institute, Yale University, New Haven, CT 06520, USA. ³QUANTIC team, INRIA de Paris, 2 Rue Simone Iff, 75012 Paris, France.

*These authors contributed equally to this work.

†Corresponding author. Email: serge.rosenblum@yale.edu

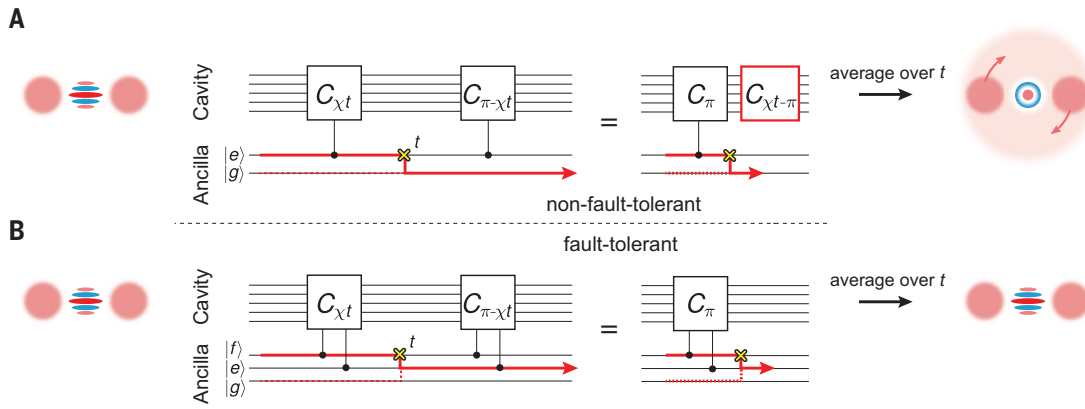


Fig. 1. Schematic circuit diagram of a FT parity measurement. Circuit schematic showing the effect of ancilla energy relaxation on a Schrödinger cat state (depicted by its Wigner tomogram, left) during a parity map in both the traditional (A) and FT (B) schemes. In these circuit diagrams, the lines within a bundle represent the individual states of the associated mode. $C_{\theta} = e^{i\theta\hat{a}^\dagger\hat{a}}$ represents a cavity phase shift of angle θ conditional

on the state of the ancilla. (A) In the non-FT implementation, an error occurring at time $t \in (0, \pi/\chi)$ results in a cavity phase shift of χt . This completely dephases the cavity state when averaged over t . (B) In the FT implementation, an error occurring at time t is equivalent to the same error occurring at the end of the parity map, because the error commutes with the interaction.

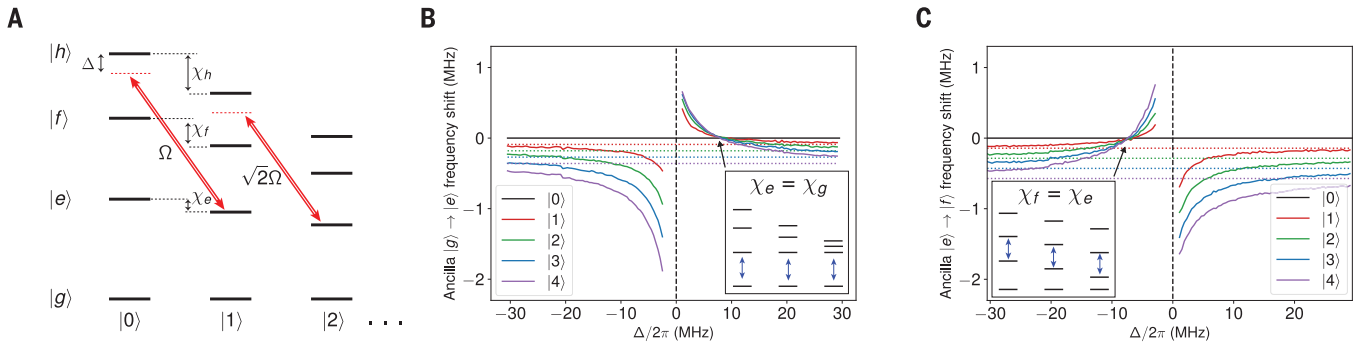


Fig. 2. Canceling the dispersive interaction with a sideband drive.

(A) Cavity-ancilla level diagram. An applied microwave tone (double red arrows) drives the $|e, n\rangle$, $|h, n-1\rangle$ transition frequency with Rabi rate $\sqrt{n}\Omega$ and detuning Δ . The resulting Stark shift changes the effective χ_e by an amount $\Omega^2/4\Delta$. (B and C) Spectroscopy of the $|g\rangle$ to $|e\rangle$ (B) and $|e\rangle$ to $|f\rangle$ (C) transitions performed with a varying number of photons in the cavity.

$\chi_{eg}(\chi_{fe})$, as well as higher-order nonlinear dispersive shifts can be extracted from the spread in transition frequencies with respect to photon number (see supplementary text 3). The indicated crossing points show where $\chi_{eg}(\chi_{fe})$ is approximately zero, as emphasized by the blue arrows in the insets depicting the effective level diagram. The dotted lines refer to the transition frequencies when no sideband drive is applied.

while removing relaxation-induced dephasing by choosing a large value of χ_{fg} , and $\chi_{fe} = 0$. The desired FT interaction Hamiltonian is therefore

$$\hat{H}_{\text{int}}^{\text{FT}} = \chi_f \hat{a}^\dagger \hat{a} (|e\rangle\langle e| + |f\rangle\langle f|) \quad (2)$$

which clearly commutes with ancilla relaxation from $|f\rangle$ as well as dephasing events.

In our solution, χ_{fg} is fixed by our sample geometry, and we achieve $\chi_{fe} = 0$ by tuning χ_e in situ. Our tuning is implemented by using a sideband tone at a detuning Δ from the resonant frequency $\omega_{\text{res}} = \omega_{he} - \omega_c = 2\pi \times 8\text{GHz}$. This results in a driven sideband term $\hat{H}_d = \frac{\Omega}{2} \hat{a}^\dagger |e\rangle\langle h| e^{i\Delta t} + \text{h.c.}$, which couples the levels $|e, n\rangle$ and $|h, n-1\rangle$ (18, 19), with n the number of cavity photons and $|h\rangle$ the third excited ancilla state (Fig. 2A). For the drive amplitude used throughout this experiment, the single-photon Rabi oscillation rate is $\Omega =$

$2\pi \times 1.7\text{MHz}$ when $\Delta = 0$ (see supplementary text 2). When sufficiently detuned ($\Delta \gg \Omega$), we can approximate this time-dependent Hamiltonian with the time-independent effective interaction:

$$\hat{H}_{\text{eff}} = \frac{\Omega^2}{4\Delta} [\hat{a}^\dagger |e\rangle\langle h|, \hat{a} |h\rangle\langle e|] = \chi_e^{\text{ind}} [(|e\rangle\langle e| - |h\rangle\langle h|) \hat{a}^\dagger \hat{a} - |h\rangle\langle h|] \quad (3)$$

to first order (see supplementary text 3), where $\chi_e^{\text{ind}} = \Omega^2/4\Delta$. In our experiment, $|h\rangle$ is never occupied, and therefore terms involving $|h\rangle$ can be ignored, leaving a Hamiltonian that has exactly the form of a dispersive interaction, conditioned on the ancilla being in $|e\rangle$. By choosing the detuning, one can engineer an induced χ_e^{ind} with either positive or negative sign. Therefore, we consider the total interaction Hamiltonian $\hat{H}_{\text{int}} = \hat{H}_{\text{int}}^0 + \hat{H}_{\text{eff}}$ and the associated dispersive interaction rates $\chi_j = \chi_j^0 + \chi_j^{\text{ind}}$, where the

zero index refers to the undriven case. This allows for the total cancellation of either χ_{eg}^0 (at $\Delta = 2\pi \times 9.3\text{MHz}$, Fig. 2B) or χ_{fe}^0 (at $\Delta = 2\pi \times -6.4\text{MHz}$, Fig. 2C), leaving only the higher-order nonlinear dispersive shift of order $\Omega^4/\Delta^3 \ll \chi_e^0, \chi_f^0$ (see supplementary text 3).

The potential of this approach can be demonstrated by using the tunable cavity-ancilla interaction to suppress ancilla-induced shot noise dephasing in the cavity (20). We achieve this by choosing a detuning such that $\chi_e^{\text{ind}} = -\chi_{eg}^0$, yielding $\chi_{eg} = 0$ (Fig. 3A). This choice of detuning prevents thermal ancilla excitations from $|g\rangle$ to $|e\rangle$ (which occur on average once every 1.1 ms) from dephasing the cavity, resulting in a marked increase in the coherence time of a cavity-encoded qubit (Fig. 3B). If we prepare an initial state $(|0\rangle + |1\rangle)|g\rangle$ and turn on the sideband drive with a variable detuning, we can measure the cavity coherence time (T_2^c) as a function of χ_{eg} . The dephasing time $T_\phi^c(\chi_{eg}) \equiv [1/T_2^c(\chi_{eg}) - 1/(2T_1^c)]^{-1}$

inferred from these data increases from $T_{\phi}^c(\chi_{eg}^0) = 1.1 \pm 0.1$ ms to $T_{\phi}^c(0) = 14 \pm 1$ ms when $\chi_{eg} = 0$ (Fig. 3B). This demonstration not only showcases the effectiveness of the drive in canceling the system-ancilla interaction, but also shows that the addition of the drive does not produce unwanted cavity decoherence at an appreciable level.

Next, we construct the FT parity measurement protocol by choosing the appropriate detuning Δ , such that $\chi_e^{\text{ind}} = +\chi_{fe}^0$ and therefore $\chi_{fe} = 0$. In this case, we realize the Hamiltonian of Eq. 2, for which ancilla relaxation from $|f\rangle$ to $|e\rangle$ does not change the evolution of the cavity. To qualitatively demonstrate the resulting fault tolerance, we follow the protocol in Fig. 4A with $N = 1$. In this experiment, we first prepare an even Schrödinger cat state with mean photon number two in the cavity (see supplementary text 5). We then map the photon-number parity onto the ancilla in three different ways (Fig. 4, B to D), as outlined below. We measure the ancilla to determine the outcome of the parity measurement and reset it to the ground state. Finally, we perform Wigner tomography on the cavity to determine the fidelity of the final cavity state conditioned on the outcome of the parity measurement. To focus on ancilla-induced errors, we filter out instances in which a photon loss event occurred (see supplementary text 6).

We demonstrate the advantage of the FT protocol (Π_{FT}) by comparing it with two alternative protocols: the traditional parity measurement (Π_{ge}), which uses a $|g\rangle + |e\rangle$ encoding in the ancilla, and Π_{gf} , which uses a $|g\rangle + |f\rangle$ encoding but without applying the sideband drive that zeroes χ_{fe} . All three protocols have similar parity assignment fidelities of 83, 86.5, and 82% for Π_{ge} , Π_{gf} , and Π_{FT} , respectively. In the absence of photon loss, the outcome of the parity measurement indicates specific ancilla events during the parity mapping (see supplementary text 7). In the traditional Π_{ge} protocol, the outcome is either $|g\rangle$ or $|e\rangle$ (Fig. 4B). No-error events result in $|g\rangle$, whereas ancilla dephasing events lead the ancilla to end up in $|e\rangle$. Relaxation errors cannot be singled out, as they result in a detection of $|g\rangle$ or $|e\rangle$ with equal probability. Relaxation errors therefore manifest as a lowered fidelity of the cavity state for both outcomes, a direct consequence of non-fault-tolerance. We next perform the Π_{gf} protocol, without applying the sideband drive (Fig. 4C). To initialize the ancilla in a $|g\rangle + |f\rangle$ superposition, we use a g - e $\pi/2$ -pulse followed by a e - f π -pulse. We then allow the system to evolve under the interaction Hamiltonian for a time $\pi/\chi_{fg}^0 \sim 2$ μs so that the cavity phase space acquires a π rotation conditional on the photon-number parity. After applying the reverse of the ancilla preparation sequence, the ancilla is in state $|g\rangle$ if no ancilla error has occurred. If a dephasing error occurs, the ancilla ends up in $|e\rangle$. In contrast to the Π_{ge} protocol, we can now distinguish relaxation events, for which the ancilla ends up in $|f\rangle$. It is now evident that dephasing events do not affect the cavity state (Fig. 4C), whereas a relaxation event, which does

Fig. 3. Improving the cavity coherence time by decoupling the cavity from thermal ancilla excitations.

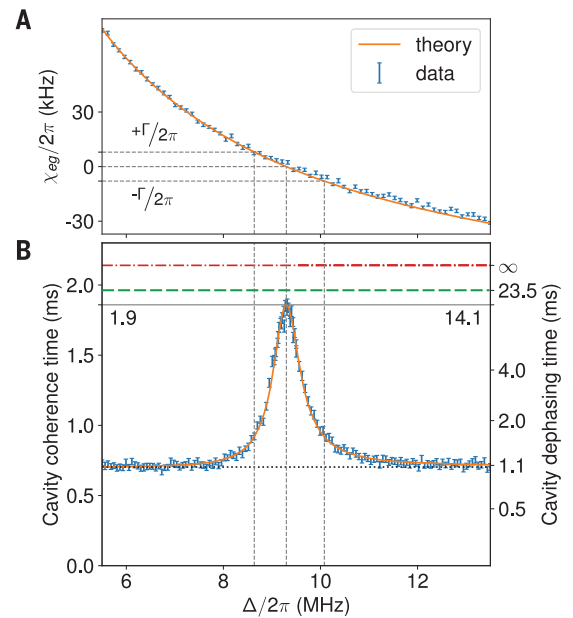
Whereas a bare cavity is nearly completely limited by single-photon loss, a cavity dispersively coupled to an ancilla experiences dephasing because of spontaneous ancilla excitations.

(A) The measured dispersive interaction (blue markers) varies as a function of sideband drive detuning from resonance Δ as $\chi_{eg} = \chi_{eg}^0 + \Omega^2/4\Delta$ (solid orange line).

(B) Cavity coherence times as a function of the sideband drive frequency obtained from cavity Ramsey experiments. In the absence of quantum error correction, the cavity coherence time is limited to $2T_1^c \sim 2.2$ ms (red dot-dashed line).

Without sideband drive, thermal ancilla excitations limit the cavity coherence to about 700 μs (dotted black line).

Protection against these excitations starts occurring when $|\chi_{eg}| < \Gamma/2\pi$ (dashed gray lines), where $\Gamma = 1/T_1^{eg}$ is the ancilla $|e\rangle$ to $|g\rangle$ decay rate. This dephasing source is almost entirely removed for $\chi_{eg} = 0$, resulting in a coherence time $T_2^c(\chi_{eg} = 0) = 1.9$ ms (solid gray line), close to the ~ 2 -ms limit set by second-order thermal excitation from $|e\rangle$ to $|f\rangle$ (dashed green line). The analytical behavior of the cavity coherence (orange line, see supplementary text 4) closely matches the observed values.



not commute with the interaction, dephases the cavity state.

Finally, we perform the FT parity mapping Π_{FT} (Fig. 4D). In addition to the sequence of the Π_{gf} protocol, we now also apply the sideband drive so that $\chi_{fe} = 0$ in the time period between the two e - f π -pulses. In this case, we see that the cavity coherence is maintained even in the case of ancilla relaxation. The modest increase in the prevalence of dephasing events is a result of a slightly degraded ancilla dephasing time in the presence of the strong drive.

In an error-correction setting, the parity of the logical qubit must be repeatedly measured. To demonstrate the advantage supplied by the FT parity measurement in this context, we use the protocol indicated in Fig. 4A and extract the final state fidelity as a function of the number of measurements (N). With an exponential fit, we can assign a characteristic number of measurements (N_0) in which the cavity fidelity decays. At this point, we can quantify the improvement offered by the FT protocol. We see that $N_0(\Pi_{gf})/N_0(\Pi_{ge}) = 2.6 \pm 0.2$, showing that even without sideband drive, the Π_{gf} protocol offers some advantages compared to Π_{ge} . The first reason is that the probability of relaxation is lower for Π_{gf} , because the relaxation time of $|f\rangle$ (24 μs) is nearly the same as that of $|e\rangle$ (26 μs), whereas the parity measurement time of Π_{gf} (as well as Π_{FT}) is less than half that of Π_{ge} . The second reason is that the cavity is less dephased given that an ancilla relaxation event occurred, because the cavity angle is distributed between 0 and $\pi\chi_{fe}^0/\chi_{fg}^0 = 0.6\pi$ (as evident from the residual coherence after a relaxation event in Fig. 4C). The

FT implementation improves on Π_{gf} by a factor of 2.0 ± 0.1 , resulting in a total fault-tolerance gain of $N_0(\Pi_{\text{FT}})/N_0(\Pi_{ge}) = 5.1 \pm 0.3$. We can compare the observed cavity dephasing rates with predictions for residual uncorrected errors, the largest of which are thermal excitation during the parity map and decay during readout (see supplementary text 9). Monte Carlo simulations (see supplementary text 8) of how the cavity phase distribution is affected by these factors produce fidelity decay curves that are in good agreement with the observed results. The agreement is best in the case of the non-FT measurements, where cavity dephasing is dominated by a single well-understood mechanism, namely, ancilla decay during the parity map. The simulation underestimates the decay in the FT case, indicating that there are additional mechanisms for dephasing that are not captured in our model. Some of these mechanisms may be explained by ancilla decoherence induced by the strong sideband drive.

It is worth emphasizing the distinction between the FT implementation of an operation, as demonstrated here, and FT quantum computing architectures. Whereas the former is assessed in terms of reduction of error propagation, the latter is commonly interpreted as the presence of an error threshold, below which the error rate of a system scales favorably with system size. Any FT architecture must contain FT syndrome measurements, and therefore they are a necessary step toward realizing such a system.

We expect FT quantum error correction based on the presented scheme to substantially enhance the lifetime of a logical qubit. Further desired

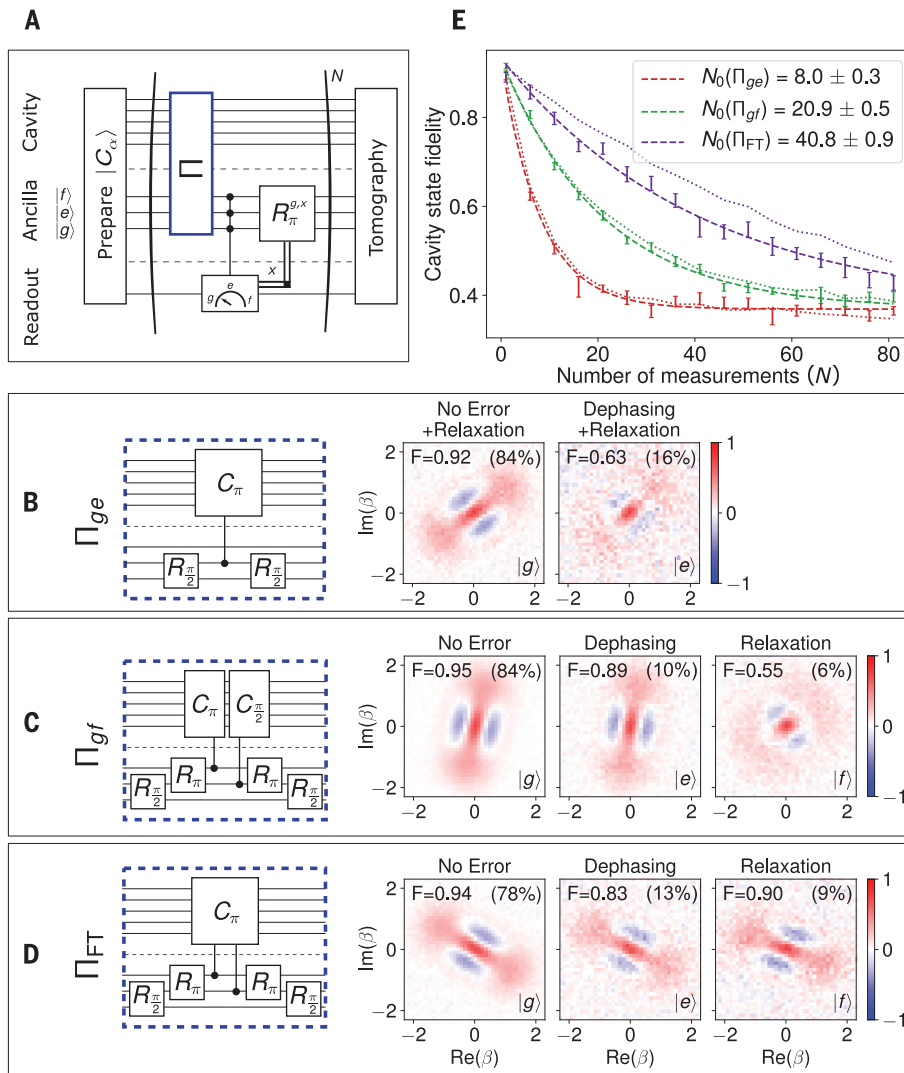


Fig. 4. Demonstration of a fault-tolerant parity measurement. (A) Circuit protocol characterizing the parity syndrome measurement and tomography (see supplementary text 5 and 6) of the resulting cavity state. We start by initializing the cavity in $|C_\alpha\rangle$. After every parity map Π (indicated in blue), we perform a three-outcome ancilla readout and reset the ancilla using π -pulses (R_π). The parity measurements are implemented in three different ways as shown in (B) to (D). To focus on ancilla errors, the tomography includes parity measurements used to filter out photon loss. (B to D). Wigner tomography of the cavity state conditioned on the outcome of a single parity measurement ($N = 1$). The outcome (shown in the bottom right of each Wigner plot) informs us about ancilla behavior during the parity mapping (top, see supplementary text 7). The prevalence of this outcome is indicated in the top right. For each Wigner tomogram, a state fidelity F (shown in the top left) is given, each with statistical error smaller than 0.01. The fidelity of the initial cat state is ~ 0.95 owing to imperfections in state preparation and tomography. For Π_{ge} (B) and Π_{gf} (C), ancilla relaxation results in a depurated cavity state, whereas for Π_{FT} (D), the logical qubit is preserved. (E) Fidelity versus number of measurements (N) for the three types of parity measurement. The dotted lines are simulated fidelities extracted from Monte Carlo trajectories (see supplementary text 8), and the dashed lines are exponential fits to the data $F(N) = Ae^{-N/N_0} + c$ with $A \sim 0.56$ and $c \sim 0.37$ for all curves.

improvements are a decreased parity measurement time and extension to higher orders of FT protection. For instance, by using four instead of three ancilla levels, we can protect against relaxation errors up to second order, or alterna-

tively, against both relaxation and thermal excitations to first order. However, more study is needed to allow for the required increase in drive power without degrading the system coherence.

Although our results were demonstrated in the context of cat-code error correction, the methods used are applicable in a broader context. In many other implementations, the used qubits are in effect nonlinear multilevel systems, whose interactions can be modified with similar techniques. Introducing symmetries in those interactions as a hardware-efficient approach to fault tolerance can reduce the complexity required for minimizing the spread of errors from component to component.

REFERENCES AND NOTES

1. M. Nielsen, I. Chuang, *Quantum Computation and Quantum Information* (Cambridge Univ. Press, 2010).
2. E. Knill, R. Laflamme, W. H. Zurek, *Proc. R. Soc. Lond. A* **454**, 365–384 (1998).
3. D. P. DiVincenzo, P. W. Shor, *Phys. Rev. Lett.* **77**, 3260–3263 (1996).
4. B. Eastin, E. Knill, *Phys. Rev. Lett.* **102**, 110502 (2009).
5. A. G. Fowler, M. Mariantoni, J. M. Martinis, A. N. Cleland, *Phys. Rev. A* **86**, 032324 (2012).
6. D. Gottesman, Quantum fault tolerance in small experiments. arXiv:1610.03507 [quant-ph] (2016).
7. P. Aliferis, A. W. Cross, *Phys. Rev. Lett.* **98**, 220502 (2007).
8. N. M. Linke et al., *Sci. Adv.* **3**, e1701074 (2017).
9. M. Takita, A. W. Cross, A. D. Córcoles, J. M. Chow, J. M. Gambetta, *Phys. Rev. Lett.* **119**, 180501 (2017).
10. E. Kapit, *Phys. Rev. Lett.* **120**, 050503 (2018).
11. D. A. Lidar, I. L. Chuang, K. B. Whaley, *Phys. Rev. Lett.* **81**, 2594–2597 (1998).
12. B. Vlastakis et al., *Science* **342**, 607–610 (2013).
13. Z. Leghtas et al., *Phys. Rev. Lett.* **111**, 120501 (2013).
14. M. Mirrahimi et al., *New J. Phys.* **16**, 045014 (2014).
15. L. Sun et al., *Nature* **511**, 444–448 (2014).
16. M. Brune, S. Haroche, V. Lefevre, J. M. Raimond, N. Zagury, *Phys. Rev. Lett.* **65**, 976–979 (1990).
17. N. Ofek et al., *Nature* **536**, 441–445 (2016).
18. S. Rosenblum et al., *Nat. Commun.* **9**, 652 (2018).
19. S. Zeytinoglu et al., *Phys. Rev. A* **91**, 043846 (2015).
20. G. Zhang, Y. Liu, J. J. Raftery, A. A. Houck, *npj Quantum Inf.* **3**, 1 (2017).

ACKNOWLEDGMENTS

We thank L. Herviou for contributing to the idea of using higher transmon levels. We thank I. Chuang and S. Girvin for helpful discussions, C. S. Wang and S. Mundhada for reviewing the manuscript, and N. Ofek for providing the logic for the field programmable gate array (FPGA) used for the control of this experiment. **Funding:** This research was supported by the U.S. Army Research Office (W911NF-14-1-0011). P.R. was supported by the U.S. Air Force Office of Scientific Research (FA9550-15-1-0015), and L.J. by the Alfred P. Sloan Foundation and the Packard Foundation. Facilities use was supported by the Yale Institute for Nanoscience and Quantum Engineering (YINQE), the Yale SEAS cleanroom, and the National Science Foundation (MRSEC DMR-1119826). **Author contributions:** S.R., P.R., M.M., L.J. and R.J.S. devised the original concept. S.R., P.R., and L.F. fabricated the device. S.R. and P.R. performed the measurements and data analysis. M.M. and L.J. provided theoretical contributions. S.R., P.R., and R.J.S. wrote the manuscript with contributions from all authors. R.J.S. supervised the project. **Competing interests:** L.F. and R.J.S. are cofounders, shareholders, members of the scientific advisory board, and paid consultants of Quantum Circuits, Inc. S.R., P.R., L.F., L.J., and R.J.S. are co-inventors on a patent application related to this work. **Data and materials availability:** All data are provided in the manuscript or the supplementary materials.

SUPPLEMENTARY MATERIALS

www.sciencemag.org/content/361/6399/266/suppl/DC1
Supplementary Text
Figs. S1 to S4
Tables S1 to S4
References (21–23)

28 February 2018; accepted 22 May 2018
10.1126/science.aat3996

Fault-tolerant detection of a quantum error

S. Rosenblum, P. Reinhold, M. Mirrahimi, Liang Jiang, L. Frunzio and R. J. Schoelkopf

Science **361** (6399), 266-270.
DOI: 10.1126/science.aat3996

Fault-tolerant quantum coding

Noise and imperfections in a quantum system can result in the presence and propagation of errors through the system. A reliable quantum processor will need to be able to correct for these errors and error syndromes. Rosenblum *et al.* used higher quantum states of a superconducting-based quantum circuit to demonstrate a method for the fault-tolerant measurement of an error-correctable logical qubit. Such fault-tolerant measurements will allow more frequent interrogations of the state of the logical qubit, ultimately leading to the implementation of more quantum operations and more complex entangled quantum circuits.

Science, this issue p. 266

ARTICLE TOOLS

<http://science.sciencemag.org/content/361/6399/266>

SUPPLEMENTARY MATERIALS

<http://science.sciencemag.org/content/suppl/2018/07/18/361.6399.266.DC1>

REFERENCES

This article cites 20 articles, 3 of which you can access for free
<http://science.sciencemag.org/content/361/6399/266#BIBL>

PERMISSIONS

<http://www.sciencemag.org/help/reprints-and-permissions>

Use of this article is subject to the [Terms of Service](#)